ChemInform Abstract: Molecular Germanium Selenophosphate Salts: Phase-Change Properties and Strong Second Harmonic Generation.

ARTICLE *in* JOURNAL OF THE AMERICAN CHEMICAL SOCIETY · NOVEMBER 2012

Impact Factor: 12.11 · DOI: 10.1021/ja309386e · Source: PubMed

JACS
JOURNAL OF THE AMERICAN CHEMICAL SOCIETY
Article
pubs.acs.org/JACS

Molecular Germanium Selenophosphate Salts: Phase-Change Properties and Strong Second Harmonic Generation

Collin D. Morris,[†] In Chung,[†] Sungoh Park,[‡] Connor M. Harrison,[‡] Daniel J. Clark,[‡] Joon I. Jang,[‡] and Mercouri G. Kanatzidis*[,†]

[†]Department of Chemistry, Northwestern University, Evanston, Illinois 60208, United States

[‡]Department of Physics, Applied Physics and Astronomy, State University of New York (SUNY) at Binghamton, Binghamton, New York 13902, United States

Supporting Information

ABSTRACT: A new series of germanium chalcophosphates with the formula $A_4GeP_4Q_{12}$ (A = K, Rb, Cs; Q = S, Se) have been synthesized. The selenium compounds are isostructural and crystallize in the polar orthorhombic space group $Pca2_1$. The sulfur analogues are isostructural to one another but crystallize in the centrosymmetric monoclinic space group $C2/c$. All structures contain the new molecular anion $[GeP_4Q_{12}]^{4-}$; however, the difference between the sulfides and selenides arises from the change in crystal packing. Each discrete molecule is comprised of two ethane-like P_2Q_6 units that chelate to a central tetrahedral Ge^{4+} ion in a bidentate fashion. The selenides were synthesized pure by stoichiometric reaction of the starting materials, whereas the sulfides contained second phases. The band gaps of the molecular salts are independent of the alkali metal counterions and have a value of 2.0 eV for the selenides and 3.0−3.1 eV for the sulfides. All $A_4GeP_4Se_{12}$ compounds melt congruently, and the potassium analogue can be quenched to give a glassy phase that retains its short-range order as shown by Raman spectroscopy and powder X-ray diffraction. Interestingly, $K_4GeP_4Se_{12}$ is a phase-change material that reversibly converts between glassy and crystalline states and passes through a metastable crystalline state upon heating just before crystallizing into its slow-cooled form. Initial second harmonic generation (SHG) experiments showed crystalline $K_4GeP_4Se_{12}$ outperforms the other alkali metal analogues and exhibits the strongest second harmonic generation response among reported quaternary chalcophosphates, ∼30 times that of $AgGaSe_2$ at 730 nm. A more thorough investigation of the nonlinear optical (NLO) properties was performed across a range of wavelengths that is almost triple that of previous reports (λ = 1200−2700 nm) and highlights the importance of broadband measurements. Glassy $K_4GeP_4Se_{12}$ also exhibits a measurable SHG response with no poling.

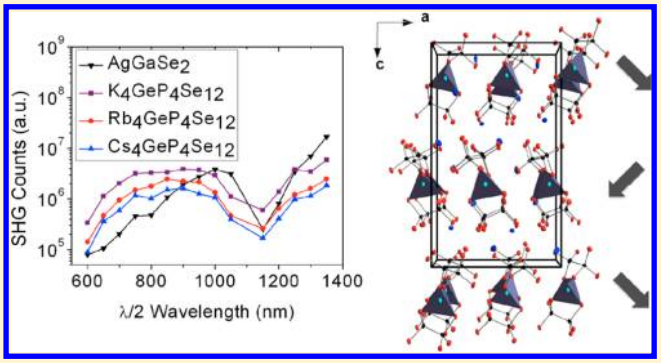

INTRODUCTION

New materials are of primary importance as technologies evolve and more stringent requirements are demanded. Chalcophosphates have proven to be promising candidates in areas that entail such properties as ferroelectricity,[1−3] photoluminescence,[4−6] reversible crystal-to-glass phase transitions,[5,7,8] superionic conductors,[9,10] and second harmonic generation (SHG).[4,7,11−13] The wide structural diversity exhibited by these compounds also merits exploration in this area since new and interesting phases continue to be discovered.[14−24] Infrared nonlinear optical (IR-NLO) materials that can generate a coherent beam of radiation between 3 and 14 μm are highly sought after for use in the environmental monitoring of toxic gases,[25,26] high-precision surgery via laser ablation of biotissue,[27,28] detection of breath biomarkers,[29] telecommunications,[30,31] and standoff detection of explosives.[32] Currently used IR-NLO materials such as $AgGaQ_2$ (Q = S, Se) and $ZnGeP_2$ exhibit several of the necessary properties required of NLO materials; however, low laser-induced damage thresholds or two-photon absorption (TPA) are problems that are encountered as well.[33−39] Chalcophosphates, and chalcogenides in general, are promising for NLO applications in the mid-IR, a region in which they are commonly transparent, and are far superior to well-studied oxides that tend to have lower efficiencies and absorption bands in this area of the spectrum.[40] Ternary chalcophosphates such as $K_2P_2Se_6$ and $KPSe_6$ show exceptionally strong SHG response in the visible/near-IR region as compared to benchmark chalcopyrite materials $AgGaQ_2$ (Q = S, Se). $KPSe_6$ has the added benefit of exhibiting excellent SHG response in melt-drawn optical glassy fibers as well as being solution processable in *N*,*N*-dimethylformamide to obtain highly nonlinear crystalline thin films with strong SHG and DFG (difference frequency generation) efficiencies.[7,11,13] Chalcogenide glasses are also an important family of materials and find use in areas such as phase-change random

Received: September 21, 2012
Published: November 16, 2012

   dx.doi.org/10.1021/ja309386e | J. Am. Chem. Soc. 2012, 134, 20733−20744

access memory (PCRAM) and solar cells.[31,41−45] Because of lack of long-range order and macroscopic center of symmetry, glasses typically do not possess second-order NLO properties. Poling, however, has been utilized to prepare glasses with significant SHG responses.[46−48]

Noncentrosymmetric chalcogenides have been discovered by adding a main group or transition metal to a ternary flux that can serve to link the anionic units in novel ways.[4,12,17,49−53] Recently, we found the incorporation of Ge into a chalcophosphate structure to be a promising route for obtaining new stuctures[54] and herein report our findings of a new family of germanium chalcophosphates, both of which contain the novel molecular anion $[GeP_4Q_{12}]^{4-}$ (Q = S, Se). The sulfide analogue crystallizes in a centrosymmetric space group, whereas the selenide adopts the polar space group $Pca2_1$ and exhibits a significant NLO response in the near-IR and visible region. Our initial experiments revealed crystalline $K_4GeP_4Se_{12}$ has a maximum SHG response ∼30 times that of the benchmark material $AgGaSe_2$ at 730 nm. We were also able to extend our region of observation to a much broader wavelength range ($\lambda/2$ = 600−1350 nm) that is nearly triple that of previous SHG studies on similar compounds. Additionally, $K_4GeP_4Se_{12}$ melts congruently and was found to be a phase-change material whose melt-quenched amorphous phase undergoes an exothermic glass to crystal transition on heating. The local structure is preserved in the glassy phase, which leads to a measurable SHG response with no poling.

EXPERIMENTAL SECTION

Reagents. All reagents were used as obtained from the specified supplier: potassium metal (98%, Sigma Aldrich, St. Louis, MO); rubidium metal (99.9+%, Strem Chemicals, Inc., Newburyport, MA); cesium metal (99.9+%, Strem Chemicals, Inc., Newburyport, MA); germanium powder (99.99%, Sigma Aldrich, St. Louis, MO); red phosphorus powder (99%, Sigma Aldrich, St. Louis, MO); selenium pellets (99.99%, Sigma Aldrich, St Louis, MO); sulfur powder (99.98%, Sigma Aldrich, St. Louis, MO); *N*,*N*-dimethylformamide (ACS grade, Mallinckrodt Chemical, Phillipsburg, NJ); and diethyl ether (ACS grade, BDH Chemical, Leicestershire, U.K.). K_2Se was prepared by reaction of stoichiometric amounts of potassium and selenium in liquid ammonia as described elsewhere.[55] K_2S, Rb_2S, Cs_2S, Rb_2Se, and Cs_2Se_2 were prepared using the same procedure. P_2Se_5 was prepared by stoichiometric reaction of the elements in a 13 mm fused silica tube at 460 °C for 24 h as described elsewhere.[56]

Synthesis. All compounds were synthesized by combining the proper alkali metal chalcogenide, germanium, phosphorus, and chalcogen in the correct stoichiometric ratios in a 9 mm fused silica tube inside a nitrogen filled glovebox. The tubes were flame-sealed under vacuum (10^{-4} mbar), heated to 500 °C in 6 h, held there for 24 h, cooled to 200 °C in 24 h and then to room temperature in 3 h. The resulting products contained crystals of the target compounds. Pure products were obtained for the selenides using this method; however, unidentified impurities were observed in the sulfides even after several attempts using modified synthesis conditions and washing with polar organic solvents such as DMF.

*$K_4GeP_4Se_{12}$ (**1a**).* A mixture of 0.079 g (0.5 mmol) of K_2Se, 0.018 g (0.25 mmol) of Ge, 0.031 g (1.00 mmol) of P, and 0.197 g (2.50 mmol) of Se was added to a 9 mm fused silica tube inside a nitrogen filled glovebox. The tube was sealed under vacuum and subjected to the heating profile above. An ingot containing red, rod-like crystals of $K_4GeP_4Se_{12}$ was obtained in quantitative yield. EDS analysis on several crystals gave an average stoichiometry of $K_{4.1}Ge_{1.0}P_{4.2}Se_{11.7}$.

*Glassy $K_4GeP_4Se_{12}$ (**1b**).* A mixture of 0.079 g (0.5 mmol) of K_2Se, 0.018 g (0.25 mmol) of Ge, 0.031 g (1.00 mmol) of P, and 0.197 g (2.50 mmol) of Se was added to a 9 mm fused silica tube inside a nitrogen filled glovebox. The tube was sealed under vacuum, heated to 500 °C in 6 h, and held there for 24 h at which point it was removed from the furnace and immediately quenched in a cool water bath. EDS on several glassy samples from the red ingot gave an average stoichiometry of $K_{3.6}Ge_{1.0}P_{3.8}Se_{9.2}$.

*$Rb_4GeP_4Se_{12}$(**2**).* A mixture of 0.125 g (0.5 mmol) of Rb_2Se, 0.018 g (0.25 mmol) of Ge, 0.031 g (1.00 mmol) of P, and 0.197 g (2.50 mmol) of Se was added to a 9 mm fused silica tube inside a nitrogen filled glovebox. The tube was sealed under vacuum and subjected to the heating profile above. An ingot containing red, rod-like crystals of $Rb_4GeP_4Se_{12}$ was obtained in quantitative yield. EDS analysis on several crystals gave an average stoichiometry of $Rb_{3.9}Ge_{1.0}P_{4.3}Se_{11.6}$.

*$Cs_4GeP_4Se_{12}$ (**3**).* A mixture of 0.212 g (0.5 mmol) of Cs_2Se_2, 0.018 g (0.25 mmol) of Ge, 0.031 g (1.00 mmol) of P, and 0.158 g (2.00 mmol) of Se was added to a 9 mm fused silica tube inside a nitrogen filled glovebox. The tube was sealed under vacuum and subjected to the heating profile above. An ingot containing red, rod-like crystals of $Cs_4GeP_4Se_{12}$ was obtained in quantitative yield. EDS analysis on several crystals gave an average stoichiometry of $Cs_{3.4}Ge_{1.0}P_{4.6}Se_{12.0}$.

*$K_4GeP_4S_{12}$ (**4**).* A mixture of 0.055 g (0.5 mmol) of K_2S, 0.018 g (0.25 mmol) of Ge, 0.031 g (1.00 mmol) of P, and 0.080 g (2.50 mmol) of S was added to a 9 mm fused silica tube inside a nitrogen filled glovebox. The tube was sealed under vacuum and subjected to the heating profile above. An ingot containing pale yellow, rod-like crystals of $K_4GeP_4S_{12}$ was obtained in ∼90% yield along with a small amount of a black polycrystalline impurity with a similar stoichiometry by EDS. EDS analysis on several crystals gave an average stoichiometry of $K_{3.8}Ge_{1.0}P_{4.0}S_{11.7}$.

*$Rb_4GeP_4S_{12}$ (**5**).* A mixture of 0.102 g (0.5 mmol) of Rb_2S, 0.018 g (0.25 mmol) of Ge, 0.031 g (1.00 mmol) of P, and 0.080 g (2.50 mmol) of S was added to a 9 mm fused silica tube inside a nitrogen filled glovebox. The tube was sealed under vacuum and subjected to the heating profile above. An ingot containing pale yellow, rod-like crystals of $Rb_4GeP_4S_{12}$ was obtained in ∼90% yield along with a small amount of a black polycrystalline impurity with a similar stoichiometry by EDS. EDS analysis on several crystals gave an average stoichiometry of $Rb_{3.4}Ge_{1.0}P_{4.3}S_{11.3}$.

*$Cs_4GeP_4S_{12}$ (**6**).* A mixture of 0.149 g (0.5 mmol) of Cs_2S, 0.018 g (0.25 mmol) of Ge, 0.031 g (1.00 mmol) of P, and 0.080 g (2.50 mmol) of S was added to a 9 mm fused silica tube inside a nitrogen filled glovebox. The tube was sealed under vacuum and subjected to the heating profile above. An ingot containing pale yellow, rod-like crystals of $Cs_4GeP_4S_{12}$ was obtained in ∼90% yield along with a small amount of a black polycrystalline impurity with a similar stoichiometry by EDS. EDS analysis on several crystals gave an average stoichiometry of $Cs_{3.6}Ge_{1.0}P_{3.9}S_{11.1}$.

Single-Crystal X-ray Crystallography. Data collections were performed on a STOE IPDS II diffractometer using Mo Kα radiation (λ = 0.71073 Å) operating at 50 kV and 40 mA at 293 K. Integration and numerical absorption corrections were performed on each structure using X-AREA, X-RED, and X-SHAPE.[57] All structures were solved using direct methods and refined by full-matrix least-squares on F^2 using the SHELXTL program package.[58]

Powder X-ray Diffraction. Powder X-ray diffraction patterns were collected on ground crystalline samples of each product with a flat sample geometry using a silicon-calibrated CPS 120 INEL powder X-ray diffractometer (Cu Kα graphite-monochromatized radiation) operating at 40 kV and 20 mA equipped with a position-sensitive detector. Simulated patterns were generated using the CIF of each refined structure and the Visualizer program within FindIt.

Scanning Electron Microscopy. Images and semiquantitative energy dispersive X-ray spectroscopy (EDS) analyses were obtained using a Hitachi S-3400 scanning electron microscope equipped with a PGT energy-dipsersive X-ray analyzer. Spectra were collected using an accelerating voltage of 25 kV and a 60 s accumulation time.

Solid State UV−Vis Spectroscopy. Diffuse reflectance spectra were collected in the range of 200−2500 nm using a Shimadzu UV-3101 PC double-beam, double-monochromator spectrophotometer. The instrument was equipped with an integrating sphere and controlled by a personal computer. $BaSO_4$ was used as a standard and set to 100% reflectance. Samples were prepared by placing ground

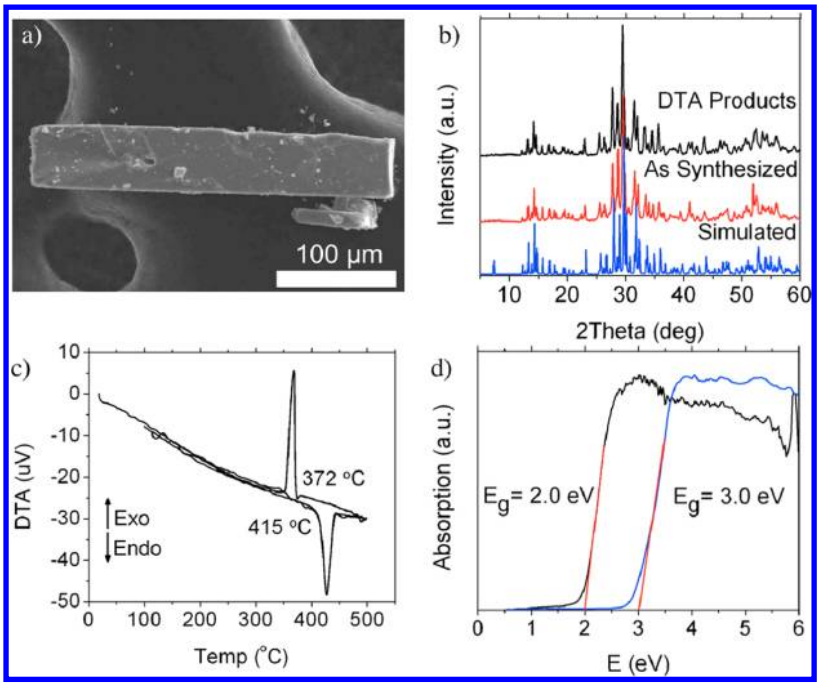

Figure 1. (a) SEM micrograph of a typical $K_4GeP_4Se_{12}$ crystal (scale bar: 100 μm). (b) PXRD of simulated (blue), as-synthesized (red), and DTA products (black) of $K_4GeP_4Se_{12}$. (c) DTA plot of $K_4GeP_4Se_{12}$ showing a single, reproducible melting, and crystallization event over two cycles and congruent melting behavior. (d) Electronic optical absorption spectra of $K_4GeP_4Se_{12}$ (black) and $K_4GeP_4S_{12}$ (blue) indicating band gaps of 2.0 and 3.0 eV, respectively.

crystalline products on a bed of $BaSO_4$. Collected reflectance data were converted to absorbance according to the Kubelka–Munk equation: $\alpha/S = (1 - R)^2/2R$, where R is the reflectance and α and S are the absorption and scattering coefficients, respectively.[55,56]

Differential Thermal Analysis. Experiments were performed using a Shimadzu DTA-50 thermal analyzer. Ground crystalline samples (~40 mg) were sealed under vacuum (~10^{-4} mbar) in a fused silica ampule. A similar amount of Al_2O_3 was sealed in a separate ampule under vacuum and used as a reference. The samples were heated and cooled at a rate of 5 °C/min to a maximum temperature of 500 °C. Two cycles of heating and cooling were performed to check the reproducibility of the obtained values. The melting and crystallization points were taken as the onset of the endothermic and exothermic peaks, respectively.

Raman Spectroscopy. Raman spectra of ground crystalline and glassy samples were collected on a DeltaNu Advantage NIR spectrometer equipped with a CCD detector using 785 nm radiation from a diode laser. The samples were loaded into borosilicate glass capillaries for the measurement. A max power of 60 mW and beam diameter of 35 μm were used. The spectrum was collected using an integration time of 10 s.

^{31}P MAS Solid-State NMR. ^{31}P magic angle spinning (MAS) NMR spectra were collected using a Varian VNMRS 400 MHz NMR. Chemical shifts are referenced to $NH_4H_2PO_4$ (δ 0.8 ppm), and coupling constants (J) are given in Hz. Pure samples of the crystalline and glassy forms of $K_4GeP_4Se_{12}$ were loaded into a 5 mm zirconia rotor, and experiments were performed using a pulse width (pwx90) of 3.5 μs and relaxation delay of 5 min. A total of 64 and 128 scans were collected for the crystalline and glassy samples, respectively, with a spin rate of 10 000 rpm for both samples.

Nonlinear Optical (NLO) Measurements. Pure samples of each selenide analogue were ground with a mortar and pestle to give a powder with a wide range of particle sizes. The powders were then mechanically sieved, resulting in eight different particle size ranges between 20 and 150 μm. Initial experiments were performed at room temperature using a reflection geometry by measuring the SHG responses from our samples as a function of the fundamental wavelength (idler beam: 1250–1800 nm) from an optical parametric amplifier (OPA), which was synchronously pumped by a frequency-tripled output (355 nm) of a Nd:YAG laser (EKSPLA PL 2143 series). The SHG signals were collected and dispersed with a Spex Spec-One 500 M spectrometer coupled to a nitrogen-cooled CCD camera.

A more thorough NLO study covering an exceptionally wide range of wavelengths was carried out at room temperature using a Horiba iHR320 spectroraph equipped with a CCD camera (Synapse) detector as well as an IGA (Symphony) dectector. Incident laser light was produced using an EKSPLA PL-2250 series diode-pumped picosecond Nd:YAG laser with a pulse width of 30 ps and a repetition rate of 50 Hz. An EKSPLA Harmonics Unit H400 was utilized along with an EKSPLA PG403-SH-DFG Optical Parametric Generator (OPG) to obtain a variety of coherent fundamental wavelengths (λ) ranging from 1200 to 4000 nm at increments of 100 nm. The CCD detector was used to measure NLO signals in the range of 600–1050 nm, and the IGA detector was employed in the 1100–2000 nm range. Spectrometer gratings of 1800, 600, and 300 grooves/mm were used for measured wavelengths in the regions of 400–850, 850–1400, and 1400–2000 nm, respectively. The output laser energy was tuned to 20 μJ using a linear polarizer before being focused onto powdered samples in capillary tubes by a conventional focusing lens (f = 75 mm). The corresponding spot size was ~0.5 mm in diameter. For the fundamental wavelengths inaccessible with 20 μJ, the NLO counts were properly scaled in accordance with the measured SHG power dependence (see, for example, Figure 10 at λ = 1200 nm). Our experimental range was limited up to 2700 nm due to significant absorption of the incident beam at the focusing lens. Also, the data at λ = 2200 nm were omitted because the pulse energy was too low. Radiated NLO signals passed through a combination of collection lenses and were guided to the spectrograph through a fiber optic bundle. SHG signals were recorded as a function of wavelength for one sample of each material with similar particle sizes (53–63 μm). SHG responses were then measured for all samples at λ = 1800 nm for particle size dependence. The relative NLO signals in a broad wavelength range were precisely calibrated with the known and measured efficiencies of all optical components.

dx.doi.org/10.1021/ja309386e | J. Am. Chem. Soc. 2012, 134, 20733–20744

Table 1. Crystallographic Refinement Details for Selenide Compounds at 293(2) K

	$K_4GeP_4Se_{12}$	$Rb_4GeP_4Se_{12}$	$Cs_4GeP_4Se_{12}$
formula weight	1300.39	1485.87	1675.63
crystal system		orthorhombic	
space group		$Pca2_1$	
crystal color		red	
unit cell dimensions	a = 13.9465(4) Å, α = 90.00°	a = 14.1881(5) Å, α = 90.00°	a = 14.3268(7) Å, α = 90.00°
	b = 7.2435(2) Å, β = 90.00°	b = 7.3566(3) Å, β = 90.00°	b = 7.6202(3) Å, β = 90.00°
	c = 24.0511(9) Å, γ = 90.00°	c = 24.2914(15) Å, γ = 90.00°	c = 24.6301(14) Å, γ = 90.00°
volume (Å^3)	2429.68(17)	2535.4(2)	2688.9(2)
Z	4		
ρ, g/cm^3	3.555	3.893	4.139
μ, mm^{-1}	20.174	26.305	22.947
F(000)	2304	2592	2880
θ range for data collection	2.81−29.00°	2.87−29.17°	2.67−29.20°
reflections collected	22 093	9700	9471
independent reflections	5819 [R_{int} = 0.0727]	5645 [R_{int} = 0.0700]	5645 [R_{int} = 0.0682]
refinement method	full-matrix least-squares on F^2		
data/restraints/parameters	5819/1/190	5645/1/190	5645/1/191
GOF	1.108	1.035	0.998
final R indices [$>2\sigma(I)$], R_1/wR_2	0.0349/0.0877	0.0561/0.0627	0.0540/0.0703
R indices (all data),[a] R_1/wR_2	0.0443/0.1178	0.0878/0.0689	0.0853/0.0767
Flack parameter	0.008(17)	0.022(19)	0.492(18)
largest diff. peak and hole	0.874 and −1.525 e Å^{-3}	1.248 and −1.081 e Å^{-3}	1.091 and −1.042 e Å^{-3}

[a] $R_1 = \sum||F_o| - |F_c||/\sum|F_o|$, $wR_2 = \{\sum[w(|F_o|^2 - |F_c|^2)^2]/\sum[w(|F_o|^4)]\}^{1/2}$ and calc $w = 1/[\sigma^2(F_o^2) + (0.0207P)^2 + 0.0000P]$, where $P = (F_o^2 + 2F_c^2)/3$.

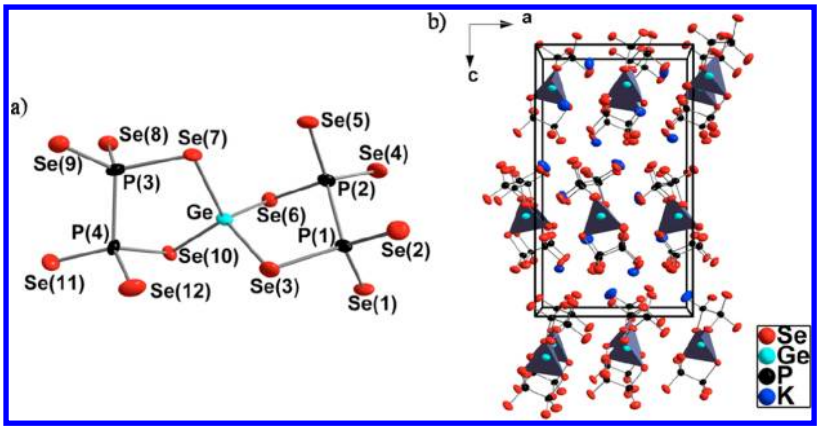

Figure 2. Discrete anionic unit (a) and extended unit cell viewed down the b-axis (b) of $K_4GeP_4Se_{12}$ with thermal ellipsoids set at 90%. The polar nature of the structure can be seen in the pointing of the tetrahedral units down the c-axis. Color code: K, dark blue; Ge, light blue; P, black; Se, red; gray polyhedra, $GeSe_4$ tetrahedral units.

RESULTS AND DISCUSSION

Synthesis and Crystal Structure Description. Red, rod-like crystals of $K_4GeP_4Se_{12}$ were first obtained from the reaction of K_2Se, Ge, P_2Se_5, and Se in a 3:6:1:12 molar ratio at 850 °C for 24 h followed by cooling to 200 °C in 100 h. Once the structure was solved and the elemental ratios determined, stoichiometric reactions were performed for the K, Rb, and Cs analogues, as well as for the corresponding sulfides, at a soaking temperature of 500 °C followed by cooling to 200 °C in 24 h and to room temperature in 3 h. Pure phases were obtained for the selenides as confirmed by the excellent match between the calculated and experimental powder X-ray diffraction (PXRD) patterns (Figures 1b, S1, S2, Supporting Information). Differential thermal analysis (DTA) experiments show a single endo- and exothermic peak at 415 and 372 °C for $K_4GeP_4Se_{12}$, 416 and 414 °C for $Rb_4GeP_4Se_{12}$, and 426 and 406 °C for $Cs_4GeP_4Se_{12}$, verifying their phase purity (Figures 1c, S1, S2, Supporting Information). The sulfides, however, all showed evidence of an unknown impurity by PXRD, and several attempts to modify the syntheses led to the same results (Figure S3, Supporting Information). Washing the as-synthesized products with polar organic solvents such as *N*,*N*-dimethylformamide, methanol, and acetonitrile also failed to affect their purity. Energy-dispersive X-ray spectroscopy (EDS) on multiple crystals of each compound gave stoichiometries close to those obtained from the single-crystal refinement.

The selenides are stable in air for several weeks, after which slight decomposition is observed on the surface of the crystals. Solubility tests were performed on the selenides under a nitrogen atmosphere. They did not dissolve or decompose in methanol or acetonitrile over the course of several days but decomposed in several hours in *N*,*N*-dimethylformamide, *N*-methylformamide, and formamide and immediately decom-

dx.doi.org/10.1021/ja309386e | J. Am. Chem. Soc. 2012, 134, 20733−20744

posed in hydrazine. Interestingly, the selenides dissolve and form a yellow solution in deionized water; however, the yellow color fades to give a colorless solution within an hour. Therefore, the compounds are water-soluble, but the $[GeP_4Se_{12}]^{4-}$ anion is most likely dismantled as the P−Se bonds and Ge−Se bonds hydrolyze. The observed insolubility of the selenides in the organic solvents may be due to the high charge on each of the anions as observed previously in similar systems.[23,24,59]

Since the selenides are isostructural to one another, $K_4GeP_4Se_{12}$ will be discussed as a representative example. The compound crystallizes in the polar orthorhombic space group $Pca2_1$ (No. 29), which belongs to the polar point group $mm2$ of the mmm Laue class, with axes of a = 13.9465(4) Å, b = 7.2435(2) Å, and c = 24.0511(9) Å (Table 1).[60,61] The structure contains the new discrete molecular unit $[GeP_4Se_{12}]^{4-}$ that is built of a central Ge^{4+} ion in a tetrahedral environment formed by two bidentate ethane-like $[P_2Se_6]^{4-}$ units (Figure 2a). All Ge−Se bonds are normal and fall in the narrow range between 2.354(2) and 2.378(1) Å (Table 2). The

Table 2. Selected Bond Lengths (Å) and Angles (deg) for $K_4GeP_4Se_{12}$ at 293(2) K with Estimated Standard Deviations in Parentheses

Se(1)−P(1)	2.121(3)	Se(10)−Ge−Se(7)	109.06(6)
Se(2)−P(1)	2.132(3)	Se(6)−Ge−Se(7)	115.52(5)
Se(3)−P(1)	2.316(3)	Se(3)−Ge−Se(7)	107.55(5)
Se(3)-Ge	2.3645(14)	Se(1)−P(1)−Se(2)	118.03(13)
Se(4)−P(2)	2.120(3)	Se(1)−P(1)−P(2)	108.29(12)
Se(5)−P(2)	2.144(3)	Se(2)−P(1)−P(2)	106.68(13)
Se(6)−P(2)	2.291(3)	Se(1)−P(1)−Se(3)	111.79(12)
Se(6)-Ge	2.3631(14)	Se(2)−P(1)−Se(3)	107.17(11)
Se(7)−P(4)	2.297(3)	P(2)−P(1)−Se(3)	103.86(12)
Se(7)−Ge	2.3778(14)	Se(4)−P(2)−Se(5)	117.22(12)
Se(8)−P(4)	2.134(3)	Se(4)−P(2)−P(1)	107.31(14)
Se(9)−P(4)	2.135(3)	Se(5)−P(2)−P(1)	112.49(13)
Se(10)−P(3)	2.320(3)	Se(4)−P(2)−Se(6)	108.67(12)
Se(10)−Ge	2.3542(15)	Se(5)−P(2)−Se(6)	108.38(12)
Se(11)−P(3)	2.116(3)	P(1)−P(2)−Se(6)	101.59(12)
Se(12)−P(3)	2.143(3)	Se(11)−P(3)−Se(12)	118.90(12)
Ge−Se(6)	2.3631(14)	Se(11)−P(3)−P(4)	107.53(13)
P(1)−P(2)	2.260(3)	Se(12)−P(3)−P(4)	110.94(13)
P(2)−Se(5)	2.144(3)	Se(11)−P(3)−Se(10)	110.28(11)
P(2)−P(1)	2.260(3)	Se(12)−P(3)−Se(10)	108.05(12)
P(3)−Se(11)	2.116(3)	P(4)−P(3)−Se(10)	99.39(11)
P(3)−P(4)	2.240(3)	Se(8)−P(4)−Se(9)	116.36(12)
P(4)−Se(8)	2.134(3)	Se(8)−P(4)−P(3)	111.40(13)
P(4)−Se(9)	2.135(3)	Se(9)−P(4)−P(3)	107.19(12)
Se(10)−Ge−Se(6)	103.56(5)	Se(8)−P(4)−Se(7)	109.81(11)
Se(10)−Ge−Se(3)	114.97(5)	Se(9)−P(4)−Se(7)	108.15(11)
Se(6)−Ge−Se(3)	106.39(5)	P(3)−P(4)−Se(7)	103.05(12)

P−Se bonds are also typical but can be divided into two groups, terminal and bridging, with the expected observation of the P−Se_b bonds being ∼0.18 Å longer than the P−Se_t bonds on average. P−Se_t bonds range from 2.116(3) to 2.144(3) Å, while those for P−Se_b are between 2.291(3) and 2.320(3) Å. The angles around Ge and P are close to those expected for tetrahedral coordination and are in the ranges of 103.56(5)−115.52(5)° and 99.4(1)−118.0(1)° for the two atoms, respectively.

The polarity of the structure, which can be seen in the arrangement of the apexes of the $GeSe_4$ tetrahedra that point along the c-axis at a ∼47° angle and is consistent with the polar point group $mm2$, arises from the 2_1 screw axis along [001] and the absence of a perpendicular mirror plane (Figure 2b). Each of the discrete molecules stacks directly on top of another along the b-axis with three short nonbonding intermolecular Se···Se interactions of 3.358(2), 3.640(1), and 3.720(2) Å forming a pseudo one-dimensional structure along the [010] direction (Figure 3a, Table 3). These distances are less than 3.80 Å, that

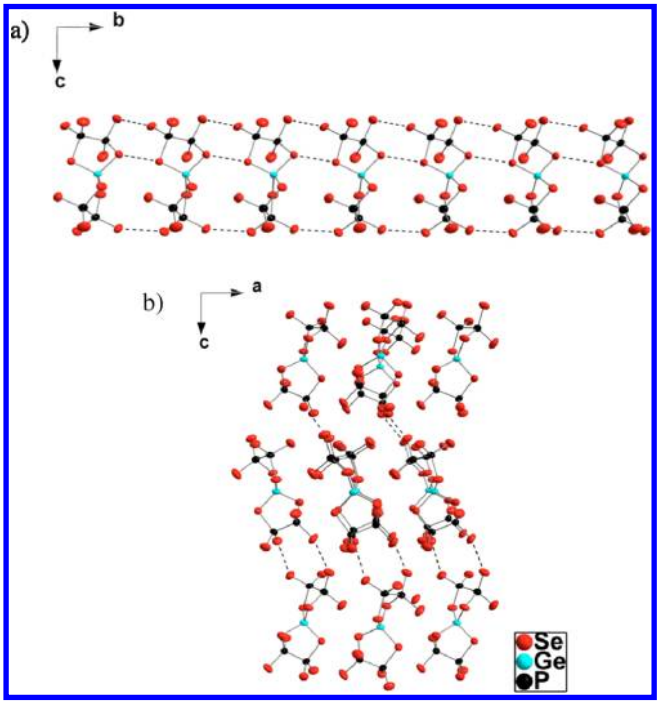

Figure 3. Intermolecular Se···Se interactions shown as dotted lines (a) along the b-axis forming a pseudo one-dimensional chain and (b) along the c-axis, with thermal ellipsoids set at 90%. K cations have been omitted for clarity. Color code: Ge, light blue; P, black; Se, red.

Table 3. Selected Intermolecular Se···Se Interactions (Å) at 293(2) K with Estimated Standard Deviations in Parentheses for $A_4GeP_4Se_{12}$[a]

label	$K_4GeP_4Se_{12}$	$Rb_4GeP_4Se_{12}$	$Cs_4GeP_4Se_{12}$	direction
Se(9)−Se(11)	3.3582(15)	3.4037(18)	3.536(2)	b
Se(7)−Se(10)	3.6404(14)	3.7027(18)	3.896(2)	b
Se(1)−Se(2)	3.7198(16)	3.791(2)	4.020(3)	b
Se(1)−Se(11)	3.6709(16)	3.720(2)	3.868(2)	c
Se(4)−Se(11)	3.7070(17)	3.785(2)	3.948(2)	c
Se(1)−Se(8)	3.7120(16)	3.835(2)	4.046(2)	c

[a]Direction identifies the axis along which the interaction occurs.

is, twice the van der Waals radii of Se, and interactions such as these have been previously observed in stabilizing the packing of molecular and polymeric selenophosphates.[12,62,63] Short nonbonding Se···Se interactions are also found between molecules along the c-axis, although their average distance is ∼0.12 Å longer than those along the b-axis. The distances between Se atoms along [001] are 3.671(2), 3.707(2), and 3.712(2) Å (Table 3). Potassium cations fill the voids between the discrete molecules to balance the negative charge with K−Se distances ranging from 3.265(4) to 3.903(4) Å. The alkali

dx.doi.org/10.1021/ja309386e | J. Am. Chem. Soc. 2012, 134, 20733−20744

Table 4. Crystallographic Refinement Details for Sulfide Compounds at 293(2) K

	$K_4GeP_4S_{12}$	$Rb_4GeP_4S_{12}$	$Cs_4GeP_4S_{12}$
formula weight	737.59	923.07	1112.83
crystal system		monoclinic	
space group		$C2/c$	
crystal color		yellow	
unit cell dimensions	a = 12.1695(8) Å, α = 90.00°	a = 12.3217(6) Å, α = 90.00°	a = 12.6475(6) Å, α = 90.00°
	b = 7.8377(5) Å, β = 100.189(6)°	b = 8.0462(3) Å, β = 100.622(4)°	b = 8.3020(3) Å, β = 102.012(4)°
	c = 23.1846(17) Å, γ = 90.00°	c = 23.5743(11) Å, γ = 90.00°	c = 24.2428(13) Å, γ = 90.00°
volume (Å^3)	2176.5(3)	2297.17(18)	2489.7(2)
Z	4		
ρ, g/cm^3	2.251	2.669	2.969
μ, mm^{-1}	3.603	11.110	8.246
F(000)	1440	1728	2016
θ range for data collection	1.78−25.00°	1.76−29.22°	1.72−29.20°
reflections collected	4569	10 664	11 630
independent reflections	1917 [R_{int} = 0.0565]	3083 [R_{int} = 0.0453]	3366 [R_{int} = 0.0396]
refinement method	full-matrix least-squares on F^2		
data/restraints/parameters	1917/0/96	3083/0/96	3366/0/96
GOF	1.058	1.136	1.026
final R indices [$>2\sigma(I)$], R_1/wR_2	0.0482/0.0639	0.0403/0.0507	0.0368/0.0591
R indices (all data),[a] R_1/wR_2	0.0771/0.0691	0.0609/0.0536	0.0606/0.0635
largest diff. peak and hole	0.469 and −0.421 e Å^{-3}	0.520 and −0.582 e Å^{-3}	0.587 and −1.187 e Å^{-3}

[a] $R_1 = \sum||F_o| - |F_c||/\sum|F_o|$, $wR_2 = \{\sum[w(|F_o|^2 - |F_c|^2)^2]/\sum[w(|F_o|^4)]\}^{1/2}$ and calc $w = 1/[\sigma^2(F_o^2) + (0.0207P)^2 + 0.0000P]$, where $P = (F_o^2 + 2F_c^2)/3$.

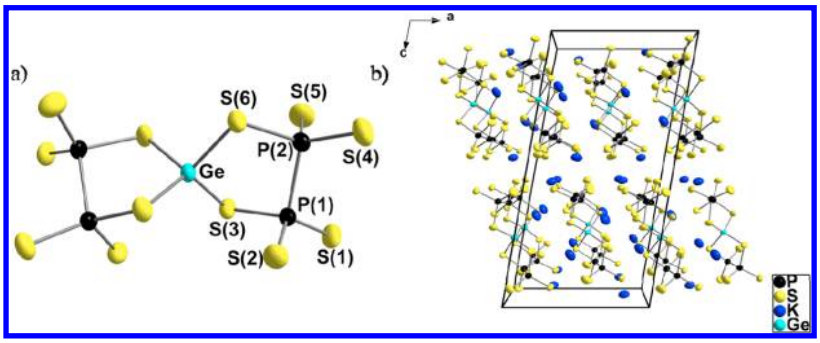

Figure 4. Discrete anionic unit (a) and extended unit cell viewed down the b-axis (b) of $K_4GeP_4S_{12}$ with thermal ellipsoids set at 70%. Color code: K, dark blue; Ge, light blue; P, black; S, yellow.

metal cations are either 7 or 8 coordinate, and all have somewhat irregular coordination geometries (Figure S4, Supporting Information).

A closer look at the other selenide analogues reveals the expected trend of increasing Se···Se distances along the b- and c-axes as the size of the alkali metal increases. Although the absolute changes are similar for the interactions along the two different axes, the percent change is greater for the Se···Se interactions along the b-axis. Also, the percent increase in the length of the b-axis is much greater as compared to the other two axes as the size of the alkali metal increases. The changes in the b-axis are 1.6% and 3.6%, whereas those for the a-axis are 1.7% and 1.0% and for the c-axis 1.0% and 1.4% in going from the K^+ to the Rb^+ and the Rb^+ to the Cs^+ analogue, respectively. The corresponding percent increase in the ionic radii of the alkali metal cations is 6.6% and 8.1%.[64] Therefore, it seems as though the pseudo one-dimensional chain along the b-axis becomes more molecular in nature as the alkali metal gets larger and decreases the intereaction between neighboring molecules.

The sulfides are also isostructural to one another, and only the potassium analogue will be discussed. $K_4GeP_4S_{12}$ crystallizes in the monoclinic space group $C2/c$ (No. 15) with axes of a = 12.1695(8) Å, b = 7.8377(5) Å, c = 23.185(2) Å, and β = 100.189(6)° (Table 4). Although the molecular anion is the same as that found in the selenium compounds, Ge sits on the special position (0, y, 1/4) of the $C2/c$ space group (Wyckoff position 4e, site symmetry 2) in $K_4GeP_4S_{12}$ (Figure 4). The second coordinating P_2S_6 ligand of the anion is generated by a 2-fold rotation axis that passes through the special position. $K_4GeP_4S_{12}$ exhibits types of trends in its bond lengths and angles similar to its selenide analogue. The Ge−S bond lengths are 2.210(1) and 2.232(1) Å, and the P−S bond lengths are 1.950(2), 1.964(2), 1.966(2), and 1.982(2) Å for P−S_t and 2.147(2) and 2.161(2) Å for P−S_b (Table S1). The angles around Ge and P are also similar and range from 98.06(7)° to 122.42(8)°. The discrete molecules again stack directly on top of one other along the b-axis; however, there are no intermolecular S···S interactions less than twice the van der Waals radii (i.e., 3.60 Å) between molecules along [010]. One short intermolecular S···S interaction of 3.431(2) Å is found along the [100] direction though.

Thermal Properties and Glass Formation. Differential thermal analysis (DTA) experiments were performed on the

dx.doi.org/10.1021/ja309386e | J. Am. Chem. Soc. 2012, 134, 20733−20744

three selenide analogues and confirm their phase purity. Single reproducible melting and crystallization points were observed when performing multiple cycles of DTA, and analysis of the products by PXRD reveals an excellent match between the calculated and pristine patterns, indicating their congruently melting behavior (Figures 1, S1, S2, Supporting Information). This, along with the relatively low melting and crystallization temperatures (415 and 372 °C for $K_4GeP_4Se_{12}$, 416 and 414 °C for $Rb_4GeP_4Se_{12}$, and 426 and 406 °C for $Cs_4GeP_4Se_{12}$), suggests that large crystals for further optical characterization can be grown using well-known growth techniques such as the Bridgman method.

Given the congruently melting behavior of these phases, a reaction for $K_4GeP_4Se_{12}$ was quenched from 500 °C into a cool water bath to investigate its glass forming ability. PXRD analysis of the quenched ingot (**1b**) revealed only broad peaks whose profile fits that of the crystalline compound, indicating that the local structure is most likely maintained but the long-range packing of the molecules has been lost (Figure 5a).

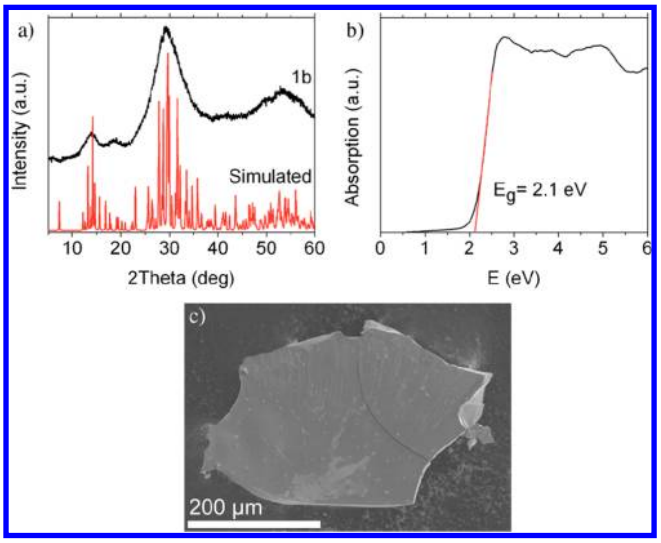

Figure 5. (a) Experimental PXRD pattern of a melt-quenched glass $K_4GeP_4Se_{12}$ sample (**1b**, black) and simulated pattern for crystalline $K_4GeP_4Se_{12}$ (red). (b) Electronic absorption spectrum of glassy $K_4GeP_4Se_{12}$. (c) SEM micrograph of glassy $K_4GeP_4Se_{12}$.

Investigation of the red-orange glassy product by EDS showed the presence of all elements with an average composition of $K_{3.5}Ge_{1.0}P_{3.8}Se_{10.9}$. Thermal analysis of the glassy phase gave unexpected results, and several different DTA experiments were run to investigate their products (**1c**–**1f**) by PXRD (Figures 6 and 7a). A single cycle of DTA to 450 °C shows two exotherms at 230 and 245 °C on heating, followed by endothermic melting at 410 °C, and crystallization on cooling at 398 °C. PXRD of the DTA product (**1c**) reveals the crystalline nature of the product and matches very well with the calculated pattern of $K_4GeP_4Se_{12}$. Two consecutive DTA cycles to 450 °C of a second sample of the glassy phase showed the same behavior as before for the first cycle. The second cycle is similar to that of the slow-cooled $K_4GeP_4Se_{12}$ and shows only a single melting and crystallization at 412 and 395 °C, respectively. Again, the PXRD of the DTA product (**1d**) is crystalline and matches with the calculated pattern. Heating a third sample of the glassy material to 325 °C confirms the reproducibility of the two exotherms on heating. PXRD of the DTA product (**1e**) matches well with the calculated pattern of the crystalline

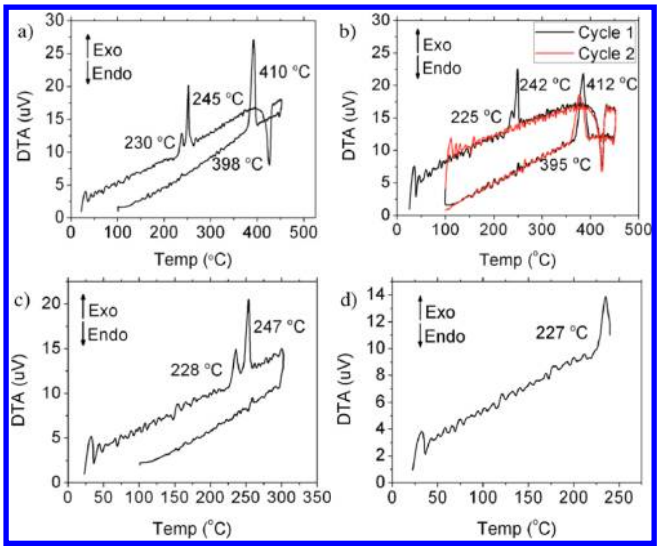

Figure 6. Differential thermal analysis (DTA) of glassy $K_4GeP_4Se_{12}$. (a) A single cycle to 450 °C (**1c**). (b) Two cycles to 450 °C (**1d**). (c) A single run to 325 °C (**1e**). (d) A single DTA run stopped just after passing through the first exotherm on heating (**1f**).

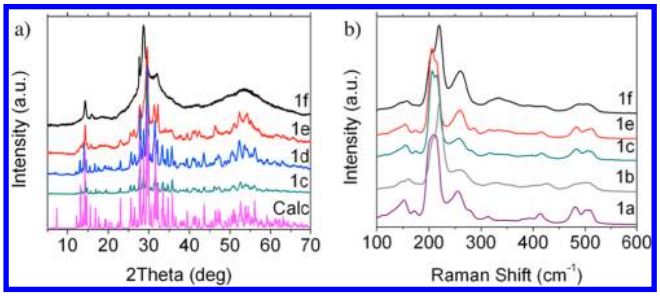

Figure 7. (a) PXRD patterns of the simulated crystalline $K_4GeP_4Se_{12}$ (pink), and DTA products **1c** (green), **1d** (blue), **1e** (red), and **1f** (black). The positions of the peaks remain unchanged for all of the samples, although their relative intensities change and have a higher background for **1e** and **1f**. (b) Raman spectra for pristine $K_4GeP_4Se_{12}$ (**1a**, purple), glassy (**1b**, gray), **1c** (green), **1e** (red), and **1f** (black). The positions of the Raman shifts remain fairly constant over all samples and do not broaden for the glassy phase.

phase, demonstrating the ability of $K_4GeP_4Se_{12}$ to convert from the glassy to the crystalline phase without melting and establishing it as a phase-change material.[41,65] Interestingly, the PXRD pattern of a fourth sample of glassy $K_4GeP_4Se_{12}$ (**1f**) heated through only the first exotherm in the DTA has peaks at the same 2θ values but with different intensities and a more amorphous background. It seems as though the glassy phase goes through a metastable crystalline state at a temperature slightly below that which results in full conversion to the most thermodynamically stable crystalline state.

Optical Absorption Spectroscopy. Optical diffuse reflectance spectra were recorded for the pure selenide compounds and the sulfide analogues containing impurities. Despite the size of the alkali metal ion increasing by ~15% in going from K^+ to Cs^+, the band gap remains at a constant value of 2.0 eV for all three selenides (Figures 1, S1, S2, Supporting Information). Therefore, the transitions between the valence and conduction bands must be based solely on the molecular anion. This is confirmed by the band gap of the glassy phase of $K_4GeP_4Se_{12}$, which is slightly higher at 2.1 eV (Figure 5b). Typically, energy band gaps are reduced when going from a

dx.doi.org/10.1021/ja309386e | J. Am. Chem. Soc. 2012, 134, 20733–20744

crystalline to a glassy phase as defect and midgap states are introduced near the band edges.[66] The fact that the band gap remains fairly constant as the long-range order is lost in the glassy phase verifies that the discrete molecular salt structure is retained. The band gaps of the sulfides remain fairly constant for the different alkali metal analogues as well (3.0 eV for K, Rb; 3.1 eV for Cs) (Figures 1, S5, Supporting Information).

Raman spectra were recorded for pristine $K_4GeP_4Se_{12}$ (**1a**) as well as for several DTA products from the experiments on glassy $K_4GeP_4Se_{12}$ (**1b**, **1c**, **1e**, and **1f**) (Figure 7b). Relatively sharp peaks at similar wavenumbers are observed in all of the spectra, and no broadening occurs for the glassy phase, which provides further evidence that the $[GeP_4Se_{12}]^{4-}$ molecular anion remains intact in the glassy phase. The shifts in the Raman spectra can be divided into three groups: the weak peaks at ~156 and 175 cm^{-1} are attributed to P_2Se_6 and $GeSe_4$ bends, the strongest peaks at ~206 and 215 cm^{-1} are attributed to the $GeSe_4$ and P_2Se_6 symmetric stretches, and those above 300 cm^{-1} arise from various asymmetric stretches of $GeSe_4$ and P_2Se_6.[8,67−69]

^{31}P NMR Spectroscopy. Ground crystalline and glassy samples of $K_4GeP_4Se_{12}$ were investigated by ^{31}P magic angle spinning (MAS) NMR. Since there are four crystallographically unique P atoms with very similar environments in the structure refinement, all of which are involved in a P−P bond, one would expect four doublets with relatively similar chemical shift values. At first glance, the spectrum of the crystalline phase appears to have only three doublets centered at δ 65.78, 61.16, and 56.81; however, the peak shape of the resonance at δ 64.97 appears to be abnormal (Figure 8). When integrating the doublets at δ 65.78, 61.16, and 56.81, values of 2.37, 1.28, and 1.00 are obtained, respectively. Therefore, the spectrum can be explained as having two doublets that overlap almost perfectly and two doublets that are shifted upfield by ~4 and 9 ppm. It is difficult to assign the four crystallographically unique P atoms to the different doublets, but their chemical shifts are in the expected region when compared to the similar molecular anion in $Cs_5P_5Se_{12}$.[8] The coupling constants for the overlapped doublets are difficult to measure but are estimated to be similar to those for the other two doublets ($J \approx 305$ Hz for δ 65.78, J = 305 Hz for δ 61.16, and J = 320 Hz for δ 56.81). The slight differences in chemical shifts and coupling constants are believed to arise from the different second nearest neighbor environments (e.g., Se−K bonds and short nonbonding Se···Se interactions) around each P atom, because the bond lengths and angles of nearest neighbors are very similar.

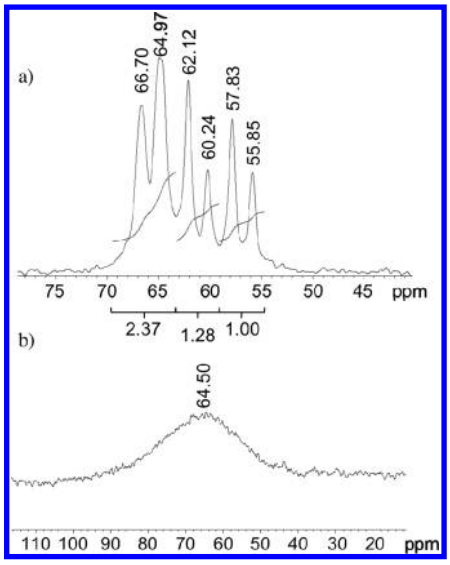

Figure 8. ^{31}P solid-state magic angle spinning (MAS) NMR spectra for crystalline (a) and glassy (b) $K_4GeP_4Se_{12}$.

The spectrum of the glassy phase shows a single broad resonance at δ 64.50. Although the molecular unit was shown to be intact in the amorphous phase by Raman spectroscopy, the loss of long-range order causes the discrete chemical shifts of the ^{31}P spectrum for the crystalline phase to inhomogeneously broaden into one.

Nonlinear Optical (NLO) Properties and Second Harmonic Generation. The *mm*2 crystal class to which the space group $Pca2_1$ belongs prompted us to perform second harmonic generation (SHG) studies on the selenium-containing compounds.[60,61] Structures of this point group are pyroelectric, optically active, and piezoelectric (i.e., exhibit SHG). A modified Kurtz and Perry powder method was first used to perform a preliminary study of the SHG response as a function of particle size for each alkali metal analogue in the range of $\lambda/2$ = 625−900 nm.[70] Ground crystalline samples were mechanically sieved into eight different particle size ranges from 20 to 150 μm. For each compound, a peak in intensity for the 45−53 μm particles was observed followed by a steady decrease in the SHG response as the particle sizes increased, indicating that all three are type-I nonphase-matchable at 760 nm (Figure S6, Supporting Information). The same trend was observed in the range of 625−900 nm of the SHG wavelength. Nonphase-matchable materials are characterized by a maximum response when the particle size is close to the average coherence length of the compound and a decrease in intensity as the particle sizes become larger.[70] Therefore, the coherence lengths, l_c, for the three compounds are assumed to be in the range of 45−53 μm. Because phase matchability is a wavelength-dependent property, it is possible that these materials are phase matchable at a different wavelength.[71]

Wavelength-dependent SHG measurements from λ = 1250−1800 nm were performed on the 45−53 μm particles, and the recorded intensities were compared to those collected for similar size particles of the benchmark IR NLO material $AgGaSe_2$ (Figure 9). $AgGaSe_2$ is also nonphase-matchable at these wavelengths, with the well-established SHG coefficient $\chi^{(2)}$ = 66 pm/V, and is a suitable reference for our materials.[72] The observed response of each chalcophosphate was

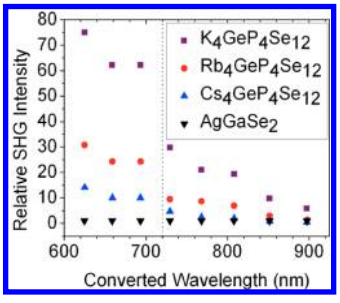

Figure 9. Relative SHG intensity of $A_4GeP_4Se_{12}$ (A = K, Rb, Cs) as compared to $AgGaSe_2$ as a function of wavelength. Intensities have been normalized to $AgGaSe_2$ at each collected wavelength. Code: $K_4GeP_4Se_{12}$ (■); $Rb_4GeP_4Se_{12}$ (●); $Cs_4GeP_4Se_{12}$ (▲); $AgGaSe_2$ (▼). The dotted line represents the absorption edge of $AgGaSe_2$ (~1.7 eV), below which a proper comparison of intensities cannot be made.

dx.doi.org/10.1021/ja309386e | J. Am. Chem. Soc. 2012, 134, 20733−20744

normalized to that of $AgGaSe_2$ at each wavelength for comparison. $K_4GeP_4Se_{12}$ exhibited the strongest signal over this entire wavelength range, followed by the Rb and Cs analogues. At 730 nm the K, Rb, and Cs analogues are ~30, 9, and 5 times stronger than $AgGaSe_2$. To the best of our knowledge, the SHG response of the K analogue is the strongest reported among quaternary chalcophosphates in this wavelength range. Although the relative intensities of the reported compounds are much greater at shorter wavelengths, comparisons below ~720 nm cannot be made due to the strong absorption of $AgGaSe_2$ ($E_g \approx 1.7$ eV).[33]

Because of the strong response of $K_4GeP_4Se_{12}$, a more thorough NLO study was performed covering a much wider wavelength range, that is, 1200−2700 nm for the fundamental wavelength. A power-dependent SHG experiment was conducted at λ = 1200 nm where two-photon absorption (TPA) of the fundamental beam can affect the observed SHG efficiency of our sample (E_g = 2.0 eV). TPA is a nonparametric NLO process and is characterized by the coefficient, β, which is proportional to the imaginary part of the third-order NLO tensor, $\chi^{(3)}$. The measured SHG responses obtained from crystalline $K_4GeP_4Se_{12}$ when the incident pulse energy was varied from 0 to 30 μJ at a fundamental wavelength of 1200 nm are shown in Figure 10a. The SHG responses as a function of

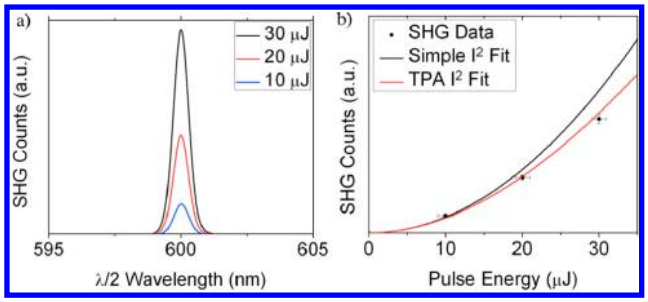

Figure 10. (a) SHG counts for 10, 20, and 30 μJ excitation pulse energies for crystalline $K_4GeP_4Se_{12}$ at λ = 1200 nm. (b) The corresponding power-dependence plot. The black curve is the predicted power dependence of the SHG when two-photon absorption is absent. The red curve is a fit to the SHG power dependence with β = 30.7 cm/GW.

pulse energy are presented in Figure 10b. Under negligible pump depletion, and in the slowly varying envelope approximation, the expression for the SHG intensity, $I(2\omega, l)$, with l being the interaction length, is given by

$$I(2\omega, l) = \frac{\omega^2 |\chi^{(2)}|^2 l^2}{2n_{2\omega} n_\omega^2 c^3 \varepsilon_0} \mathrm{sinc}^2\left(\frac{\Delta k l}{2}\right) I^2(\omega) \propto |\chi^{(2)}|^2 I^2(\omega) \quad (1)$$

where n_ω and $n_{2\omega}$ are refractive indices at ω and 2ω, respectively, c is the speed of light in vacuum, ε_0 is the vacuum dielectric constant, Δk is the phase mismatch, and $I(\omega)$ is the pump intensity. In our powder experiments based on a reflection geometry, the interaction length is the powder size, d. The solid black curve in Figure 10b corresponds to eq 1. The noticeable deviation from this simple prediction indicates that there is significant pump depletion at λ = 1200 nm. This most likely arises due to TPA of the pump beam because the fundamental wavelength is slightly over the band-to-band two-photon resonance. To rigorously explain the observed power dependence, one needs to solve coupled differential equations for the intensities at ω and 2ω considering the second-order macroscopic NLO polarization of the material and TPA simultaneously. This task usually requires numerical treatments because the NLO effects are described in terms of the electric field, whereas the TPA effects are described by the intensity. However, it is possible to estimate β by fitting the observed power dependence based on a simplified model with a modified fundamental intensity by TPA:

$$\frac{dI(\omega)}{dz} = -\beta I^2(\omega); \quad I(\omega) \rightarrow \frac{I(\omega)}{1 + \beta I(\omega) d} \quad (2)$$

where d is the powder size in the range of 53−63 μm. The red curve in Figure 10b corresponds to a least-squares fit to SHG power dependence with a single fit parameter of β = 30.7 ± 2.3 cm/GW, where the uncertainty arises from the uncertainty in the particle size. We found that this β value is reasonable considering that values for other conventional chalcogenide materials range from a few cm/GW to several hundred cm/GW.[33] For NLO applications involving beam mixing, signal amplification, and Kerr-effect-based optical switches, materials with minimal TPA, that is, low β values, are desirable.

Broadband SHG experiments were then performed on the $A_4GeP_4Se_{12}$ compounds in the range of λ = 1200−2700 nm, with a corresponding SHG wavelength, $\lambda/2$, of 600−1350 nm. Our experimental setup is quite unique in that previous studies have typically involved a fixed or limited wavelength range. We have performed experiments over a range that is almost triple that of reports on similar compounds. Although we did not use any band-pass filter for eliminating the pump beam in our SHG measurements, we confirmed that any NLO signal from the capillary tube or any other optical component is negligible in our experimental range. The NLO response of each chalcophosphate was again directly compared to that from $AgGaSe_2$.

The series of blue traces in Figure 11 show the observed SHG signals from crystalline $K_4GeP_4Se_{12}$ powders as a function of wavelength; the red traces correspond to the SHG signals from $AgGaSe_2$ under the same experimental conditions. The

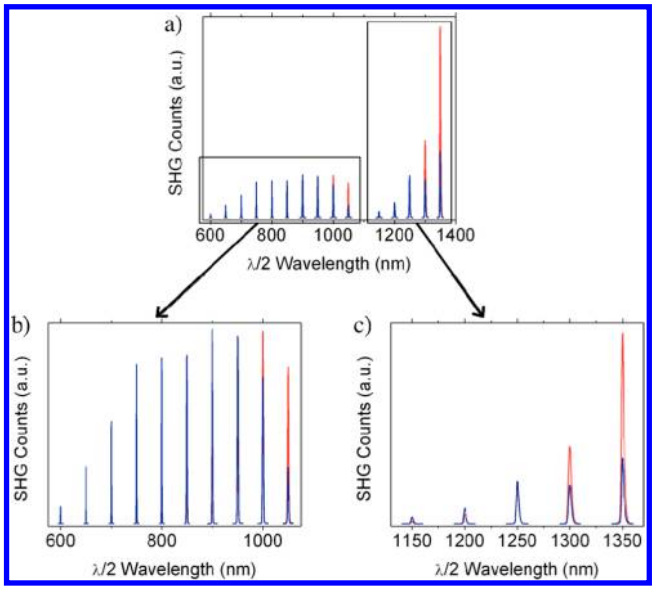

Figure 11. Wavelength-dependent SHG response for crystalline $K_4GeP_4Se_{12}$ (blue) and $AgGaSe_2$ (red) from λ = 1200−2700 nm. (b) and (c) are zoomed in regions of (a).

dx.doi.org/10.1021/ja309386e | J. Am. Chem. Soc. 2012, 134, 20733−20744

first result that is noticed is the sharp decrease in the SHG response when $\lambda/2$ approaches the optical band gaps of $K_4GeP_4Se_{12}$ and $AgGaSe_2$, ~620 and 720 nm, respectively. This occurs due to strong absorption of the produced SHG light near the band gap as well as TPA of the pump beam. Similarly, the decrease in the SHG responses in the range of $\lambda/2$ = 1000–1200 nm can be attributed to higher-order multiphoton absorption effects. Although these experiments confirm our initial results that $K_4GeP_4Se_{12}$ is a much stronger SHG material than $AgGaSe_2$ in the range of $\lambda/2$ = 600–900 nm, we see that this is not true at all longer wavelengths: $AgGaSe_2$ outperforms $K_4GeP_4Se_{12}$ at 1000 and 1050 nm; however, our material slightly outperforms $AgGaSe_2$ at 1150 and 1200 nm before their responses are essentially equal at 1250 nm and $AgGaSe_2$ becomes stronger at 1350 and 1400 nm. These results emphasize the importance of performing broadband studies because SHG responses vary widely with wavelength. Measurement at $\lambda/2$ = 1100 nm was omitted due to low pulse energy of the laser.

Figure 12 shows the relative SHG signal of all $A_4GeP_4Se_{12}$ compounds and $AgGaSe_2$ on a semilog plot. Again, the decrease

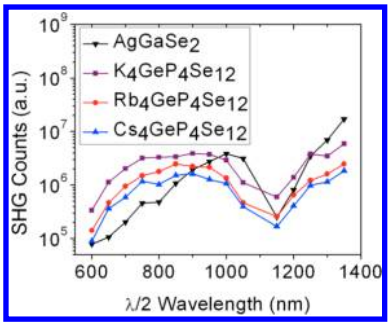

Figure 12. Broadband SHG responses of $AgGaSe_2$ (▼), $K_4GeP_4Se_{12}$ (■), $Rb_4GeP_4Se_{12}$ (●), and $Cs_4GeP_4Se_{12}$ (▲) from λ = 1200–2700 nm.

in signal at wavelengths corresponding to the band gaps of the materials and multiphoton absorptions are observed. $K_4GeP_4Se_{12}$ is confirmed to be the strongest material among the three reported chalcophosphates. On the basis of the measured wavelength-dependent NLO responses, we conclude that $|\chi^{(2)}_K/\chi^{(2)}_{Rb}| \approx 1.56$ and $|\chi^{(2)}_{Rb}/\chi^{(2)}_{Cs}| \approx 1.17$ according to eq 1. Additionally, the absolute values of the NLO tensors can be obtained by comparing them with the NLO efficiencies of the reference material, as explained below.

Figure 13 shows the particle size dependence of the measured SHG responses from $Cs_4GeP_4Se_{12}$ and $AgGaSe_2$ at a fundamental wavelength of 1800 nm. Figure 13a indicates

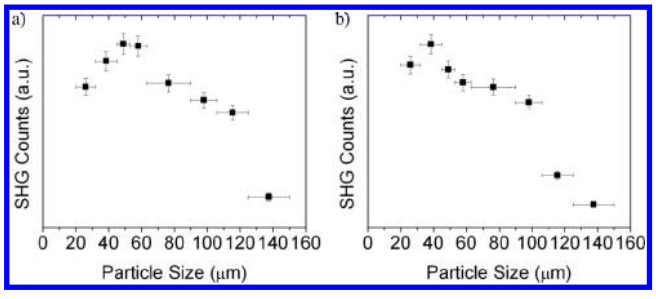

Figure 13. Particle size-dependent SHG responses from (a) $Cs_4GeP_4Se_{12}$ and (b) $AgGaSe_2$ measured at λ = 1800 nm.

that the coherence length, l_c, at this wavelength is similar to what was found previously and is about 50 μm. We also confirmed $AgGaSe_2$ is type-I nonphase-matchable at 1800 nm (Figure 13b). Because of comparable SHG counts with significant uncertainties in the 20–40 μm size range, we could not determine the corresponding coherence length of $AgGaSe_2$. However, we directly calculated $l_c = \lambda/(4|n_{2\omega} - n_\omega|) \approx 5$ μm using the measured birefringent refractive indices for $AgGaSe_2$ available elsewhere.[33] This small coherence length cannot be inferred from our powder method because the minimum accessible particle size is ~20 μm. $AgGaSe_2$ becomes phase-matchable at λ > 3000 nm, which is beyond our experimental range.

We estimated the absolute value of $\chi^{(2)}$ for $Cs_4GeP_4Se_{12}$ using eq 3 for the nonphase-matching case using $\chi^{(2)}_{ref}$ = 66 pm/V:

$$I(2\omega) \propto |\chi^{(2)}|^2 \frac{l_c^2}{2d}; \quad |\chi^{(2)}_{Cs}| = |\chi^{(2)}_{Ref}| \frac{l_{c,Ref}}{l_{c,Cs}} \left(\frac{I_{Cs}(2\omega)}{I_{Ref}(2\omega)} \right)^{1/2} \tag{3}$$

yielding $|\chi^{(2)}| \approx 6.1$ pm/V for $Cs_4GeP_4Se_{12}$. According to Figure 12, this implies that $|\chi^{(2)}| \approx 7.1$ and 11.1 pm/V for $Rb_4GeP_4Se_{12}$ and $K_4GeP_4Se_{12}$, respectively. We believe our estimations are correct within a factor of 2, where the uncertainty arises mainly from inhomogeneous distribution of powders with different sizes within the specified range.

Since glassy $K_4GeP_4Se_{12}$ was shown to retain its short-range order, SHG measurements were performed from $\lambda/2$ = 600–1350 nm (Figure 14). Although the relative efficiency is about 2

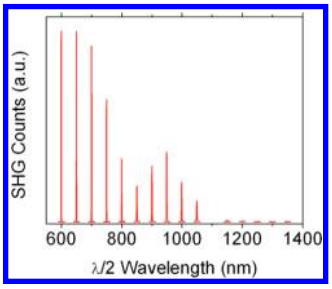

Figure 14. Wavelength-dependent SHG response from glassy $K_4GeP_4Se_{12}$.

orders of magnitude smaller than crystalline $K_4GeP_4Se_{12}$, the glassy phase exhibits a measurable SHG response (Figure 14). Contrary to conventional glassy materials, the innate second-order NLO properties of our glassy phase presumably arise because the noncentrosymmetric building blocks remain partially aligned, similar to what was observed in $KPSe_6$.[7] Interestingly, we found that the SHG efficiencies for λ > 2000 nm are strongly suppressed. This can be qualitatively explained by the fact that the short-range order present in the glassy phase will become averaged out for longer wavelengths, which in turn cancels out the SHG dipole moments.

■ CONCLUSIONS

The new family of polar selenophosphates containing the novel $[GeP_4Se_{12}]^{4-}$ molecular anion exhibits a significant second harmonic generation (SHG) response in the visible and near IR wavelength range. The response is believed to arise from the alignment of the $GeSe_4$ tetrahedra along the *c*-axis of the structure. Short nonbonding Se···Se interactions help stabilize

dx.doi.org/10.1021/ja309386e | J. Am. Chem. Soc. 2012, 134, 20733–20744

the polar character of the structure because similar intermolecular interactions are not observed in the centrosymmetric sulfur analogues. The three selenides are type-I nonphase-matchable over the investigated wavelength range, and the K^+ analogue shows a second-order NLO response ~30 times that of $AgGaSe_2$ at $\lambda/2$ = 730 nm, which, to the best of our knowledge, is the strongest among reported quaternary chalcophosphates in the range of $\lambda/2$ = 600−900 nm. It is also ~20 times stronger than $AgGaSe_2$ at the telecommunications relevant wavelength of λ = 1.55 μm. Our broadband optical measurements from λ = 1200−2700 nm roughly triple the range that has been studied in the past and demonstrate how important investigation of materials over a significantly wide range is because of their widely varying SHG efficiencies.

$K_4GeP_4Se_{12}$ is also a phase-change material that can be quenched from the melt to obtain a glassy form of the compound that, when heated below the melting point, passes through a metastable semicrystalline state before converting to the crystalline state obtained when slow cooling the melt. The amorphous phase was shown to contain intact molecular anions by Raman spectroscopy, and the metastable phase is thought to be an alternate packing of the anions that is slightly different from the slow-cooled sample. SHG measurements on glassy $K_4GeP_4Se_{12}$ also showed measurable responses that were ~2 orders of magnitude smaller than the crystalline phase with no poling. Congruently melting molecular materials such as those reported here may prove to be beneficial as phase-change materials in that once the molecule is formed only a small amount of thermal energy is required for the reorganization of the disordered molecules into an ordered crystalline state.

■ ASSOCIATED CONTENT

Supporting Information

PXRD, DTA, and UV−vis for $Rb_4GeP_4Se_{12}$ and $Cs_4GeP_4Se_{12}$, PXRD and UV−vis for the sulfides, coordination environments for K in $K_4GeP_4Se_{12}$, particle size-dependent SHG measurements, and crystallographic information files (CIF). This material is available free of charge via the Internet at http://pubs.acs.org.

■ AUTHOR INFORMATION

Corresponding Author

m-kanatzidis@northwestern.edu

Notes

The authors declare no competing financial interest.

■ ACKNOWLEDGMENTS

Financial support from the National Science Foundation (Grant DMR-1104965) is gratefully acknowledged. The SEM/EDS work was performed in the EPIC facility of NUANCE Center at Northwestern University. NUANCE Center is supported by the NSF-NSEC, NSF-MRSEC, Keck Foundation, the State of Illinois, and Northwestern University.

■ REFERENCES

(1) Carpentier, C. D.; Nitsche, R. *Mater. Res. Bull.* **1974**, *9*, 1097.
(2) Rogach, E. D.; Sviridov, E. V.; Arnautova, E. A.; Savchenko, E. A.; Protsenko, N. P. *Zh. Tekh. Fiz.* **1991**, *61*, 201.
(3) Scott, B.; Pressprich, M.; Willet, R. D.; Cleary, D. A. *J. Solid State Chem.* **1992**, *96*, 294.
(4) Banerjee, S.; Malliakas, C. D.; Jang, J. I.; Ketterson, J. B.; Kanatzidis, M. G. *J. Am. Chem. Soc.* **2008**, *130*, 12270.
(5) Chung, I.; Song, J.-H.; Kim, M. G.; Malliakas, C. D.; Karst, A. L.; Freeman, A. J.; Weliky, D. P.; Kanatzidis, M. G. *J. Am. Chem. Soc.* **2009**, *131*, 16303.
(6) Banerjee, S.; Szarko, J. M.; Yuhas, B. D.; Malliakas, C. D.; Chen, L. X.; Kanatzidis, M. G. *J. Am. Chem. Soc.* **2010**, *132*, 5348.
(7) Chung, I.; Jang, J.-I.; Malliakas, C. D.; Ketterson, J. B.; Kanatzidis, M. G. *J. Am. Chem. Soc.* **2010**, *132*, 384.
(8) Chung, I.; Jang, J. I.; Gave, M. A.; Weliky, D. P.; Kanatzidis, M. G. *Chem. Commun.* **2007**, 4998.
(9) Kamaya, N.; Homma, K.; Yamakawa, Y.; Hirayama, M.; Kanno, R.; Yonemura, M.; Kamiyama, T.; Kato, Y.; Hama, S.; Kawamoto, K.; Mitsui, A. *Nat. Mater.* **2011**, *10*, 682.
(10) Mo, Y. F.; Ong, S. P.; Ceder, G. *Chem. Mater.* **2012**, *24*, 15.
(11) Chung, I.; Malliakas, C. D.; Jang, J. I.; Canlas, C. G.; Weliky, D. P.; Kanatzidis, M. G. *J. Am. Chem. Soc.* **2007**, *129*, 14996.
(12) Chung, I.; Song, J.-H.; Jang, J. I.; Freeman, A. J.; Ketterson, J. B.; Kanatzidis, M. G. *J. Am. Chem. Soc.* **2009**, *131*, 2647.
(13) Chung, I.; Kim, M. G.; Jang, J. I.; He, J. Q.; Ketterson, J. B.; Kanatzidis, M. G. *Angew. Chem., Int. Ed.* **2011**, *50*, 10867.
(14) Kanatzidis, M. G. *Curr. Opin. Solid State Mater. Sci.* **1997**, *2*, 139.
(15) Derstroff, V.; Ensling, J.; Ksenofontov, V.; Gutlich, P.; Tremel, W. *Z. Anorg. Allg. Chem.* **2002**, *628*, 1346.
(16) Gieck, C.; Derstroff, V.; Block, T.; Felser, C.; Regelsky, G.; Jepsen, O.; Ksenofontov, V.; Gutlich, P.; Eckert, H.; Tremel, W. *Chem.-Eur. J.* **2004**, *10*, 382.
(17) Wu, Y. D.; Bensch, W. *Inorg. Chem.* **2007**, *46*, 6170.
(18) Loken, S.; Tremel, W. *Eur. J. Inorg. Chem.* **1998**, 283.
(19) Milot, S.; Wu, Y.; Nather, C.; Bensch, W.; Klepp, K. O. *Z. Anorg. Allg. Chem.* **2008**, *634*, 1575.
(20) Komm, T.; Strobel, S.; Schleid, T. *J. Alloys Compd.* **2008**, *451*, 648.
(21) Piccoli, P. M. B.; Abney, K. D.; Schoonover, J. D.; Dorhout, P. K. *Inorg. Chem.* **2001**, *40*, 4871.
(22) Hess, R. F.; Abney, K. D.; Burris, J. L.; Hochheimer, H. D.; Dorhout, P. K. *Inorg. Chem.* **2001**, *40*, 2851.
(23) Chung, I.; Holmes, D.; Weliky, D. P.; Kanatzidis, M. G. *Inorg. Chem.* **2010**, *49*, 3092.
(24) Morris, C. D.; Kanatzidis, M. G. *Inorg. Chem.* **2010**, *49*, 9049.
(25) Sorokina, I. T.; Vodopyanov, K. L. *Solid-state Mid-infrared Laser Sources*; Springer: Berlin; New York, 2003.
(26) Partnership, S. *Nat. Photonics* **2010**, *4*, 576.
(27) Serebryakov, V. A.; Boiko, E. V.; Petrishchev, N. N.; Yan, A. V. *J. Opt. Technol.* **2010**, *77*, 6.
(28) Waynant, R. W.; Ilev, I. K.; Gannot, I. *Philos. Trans. R. Soc., A* **2001**, *359*, 635.
(29) Skeldon, K. D.; Gibson, G. M.; Wyse, C. A.; McMillan, L. C.; Monk, S. D.; Longbottom, C.; Padgett, M. J. *Appl. Opt.* **2005**, *44*, 4712.
(30) Dorn, R.; Baums, D.; Kersten, P.; Regener, R. *Adv. Mater.* **1992**, *4*, 464.
(31) Eggleton, B. J.; Luther-Davies, B.; Richardson, K. *Nat. Photonics* **2011**, *5*, 141.
(32) Mukherjee, A.; Von der Porten, S.; Patel, C. K. N. *Appl. Opt.* **2010**, *49*, 2072.
(33) Nikogosyan, D. N. *Nonlinear Optical Crystals: A Complete Survey*; Springer-Science: New York, 2005.
(34) Harasaki, A.; Kato, K. *Jpn. J. Appl. Phys., Part 1* **1997**, *36*, 700.
(35) Ziegler, B. C.; Schepler, K. L. *Appl. Opt.* **1991**, *30*, 5077.
(36) Peterson, R. D.; Schepler, K. L.; Brown, J. L.; Schunemann, P. G. *J. Opt. Soc. Am. B* **1995**, *12*, 2142.
(37) Pearl, S.; Fastig, S.; Ehrlich, Y.; Lavi, R. *Appl. Opt.* **2001**, *40*, 2490.
(38) Petrov, V.; Rotermund, F.; Noack, F.; Schunemann, P. *Opt. Lett.* **1999**, *24*, 414.
(39) Song, J.; Xia, J. F.; Zhang, Z.; Strickland, D. *Opt. Lett.* **2002**, *27*, 200.
(40) (a) Sasaki, T.; Mori, Y.; Yoshimura, M.; Yap, Y. K.; Kamimura, T. *Mater. Sci. Eng., R* **2000**, *30*, 1. (b) Belokoneva, E. L.; Stefanovich, S. Y. *Journal of Solid State Chemistry* **2012**, *195*, 79. (c) Smith, M. D.;

Blau, S. M.; Chang, K. B.; Tran, T. T.; Zeller, M.; Halasyamani, P. S.; Schrier, J.; Norquist, A. J. *Journal of Solid State Chemistry* **2012**, *195*, 86. (d) West, J. P.; Hwu, S. J. *Journal of Solid State Chemistry* **2012**, *195*, 101. (e) Zhang, J. J.; Kong, F.; Xu, X.; Mao, J. G. *Journal of Solid State Chemistry* **2012**, *195*, 63. (f) Zhang, J. J.; Zhang, Z. H.; Sun, Y. X.; Zhang, C. Q.; Tao, X. T. *Journal of Solid State Chemistry* **2012**, *195*, 120. (g) Zhao, W. W.; Pan, S. L.; Wang, Y. J.; Yang, Z. H.; Wang, X.; Han, J. *Journal of Solid State Chemistry* **2012**, *195*, 73. (h) Chung, I.; Song, J. H.; Jang, J. I.; Freeman, A. J.; Kanatzidis, M. G.; Han, J. *Journal of Solid State Chemistry* **2012**, *195*, 161. (i) Lin, X. S.; Guo, Y. F.; Ye, N. *Journal of Solid State Chemistry* **2012**, *195*, 172. (j) Zhou, L. J.; Chen, L.; Li, J. Q.; Wu, L. M. *Journal of Solid State Chemistry* **2012**, *195*, 166.

(41) Raoux, S.; Welnic, W.; Ielmini, D. *Chem. Rev.* **2010**, *110*, 240.

(42) Iovu, M. S.; Colomeico, E. P.; Benea, V. G.; Popescu, M.; Lorinczi, A.; Velea, A. *J. Optoelectron. Adv. Mater.* **2011**, *13*, 1483.

(43) Wang, R. Y.; Caldwell, M. A.; Jeyasingh, R. G. D.; Aloni, S.; Shelby, R. M.; Wong, H. S. P.; Milliron, D. J. *J. Appl. Phys.* **2011**, *109*, 113506.

(44) Eom, T.; Choi, S.; Choi, B. J.; Lee, M. H.; Gwon, T.; Rha, S. H.; Lee, W.; Kim, M.-S.; Xiao, M.; Buchanan, I.; Cho, D.-Y.; Hwang, C. S. *Chem. Mater.* **2012**, *24*, 2099.

(45) Bogoslovskiy, N. A.; Tsendin, K. D. *Semiconductors* **2012**, *46*, 559.

(46) Myers, R. A.; Mukherjee, N.; Brueck, S. R. J. *Opt. Lett.* **1991**, *16*, 1732.

(47) Qiu, J. R.; Si, J. H.; Hirao, K. *Opt. Lett.* **2001**, *26*, 914.

(48) Liu, Q. M.; He, X. A.; Hu, T.; Gao, C.; Hou, Y. N.; Zhao, X. J. *Appl. Phys. A: Mater. Sci. Process.* **2011**, *102*, 245.

(49) Chen, M. C.; Wu, L. M.; Lin, H.; Zhou, L. J.; Chen, L. *J. Am. Chem. Soc.* **2012**, *134*, 6058.

(50) Zhao, H.-J.; Zhang, Y.-F.; Chen, L. *J. Am. Chem. Soc.* **2012**, *134*, 1993.

(51) Chen, M.-C.; Li, P.; Zhou, L.-J.; Li, L.-H.; Chen, L. *Inorg. Chem.* **2011**, *50*, 12402.

(52) Chen, M.-C.; Li, L.-H.; Chen, Y.-B.; Chen, L. *J. Am. Chem. Soc.* **2011**, *133*, 4617.

(53) Mei, D. J.; Yin, W. L.; Feng, K.; Lin, Z. S.; Bai, L.; Yao, J. Y.; Wu, Y. C. *Inorg. Chem.* **2012**, *51*, 1035.

(54) Morris, C. D.; Malliakas, C. D.; Kanatzidis, M. G. *Inorg. Chem.* **2011**, *50*, 10241.

(55) McCarthy, T. J.; Ngeyi, S. P.; Liao, J. H.; DeGroot, D. C.; Hogan, T.; Kannewurf, C. R.; Kanatzidis, M. G. *Chem. Mater.* **1993**, *5*, 331.

(56) Mccarthy, T. J.; Kanatzidis, M. G. *Inorg. Chem.* **1995**, *34*, 1257.

(57) Stoe & Cie. *X-AREA, X-RED, and X-SHAPE*; Darmstadt, Germany, 1998.

(58) Sheldrick, G. M. *Acta Crystallogr., Sect. A* **2008**, *64*, 112.

(59) Chondroudis, K.; Kanatzidis, M. G. *Inorg. Chem.* **1998**, *37*, 2582.

(60) Nye, J. F. *Physical Properties of Crystals: Their Representation by Tensors and Matrices*; Clarendon Press; Oxford University Press: Oxford, Oxfordshire, NY, 1984.

(61) Halasyamani, P. S.; Poeppelmeier, K. R. *Chem. Mater.* **1998**, *10*, 2753.

(62) Chung, I.; Do, J.; Canlas, C. G.; Weliky, D. P.; Kanatzidis, M. G. *Inorg. Chem.* **2004**, *43*, 2762.

(63) Bondi, A. *J. Phys. Chem.* **1964**, *68*, 441.

(64) Shannon, R. D. *Acta Crystallogr., Sect. A* **1976**, *32*, 751.

(65) Wuttig, M.; Yamada, N. *Nat. Mater.* **2007**, *6*, 824.

(66) Dhingra, S.; Kanatzidis, M. G. *Science* **1992**, *258*, 1769.

(67) Aitken, J. A.; Evain, M.; Iordanidis, L.; Kanatzidis, M. G. *Inorg. Chem.* **2002**, *41*, 180.

(68) Martin, B. R.; Dorhout, P. K. *Inorg. Chem.* **2004**, *43*, 385.

(69) Choudhury, A.; Dorhout, P. K. *Inorg. Chem.* **2006**, *45*, 5245.

(70) Kurtz, S. K.; Perry, T. T. *J. Appl. Phys.* **1968**, *39*, 3798.

(71) Boyd, R. W. *Nonlinear Optics*, 3rd ed.; Academic Press: Amsterdam; Boston, 2008.

(72) Bhar, G. C. *Jpn. J. Appl. Phys., Part 1* **1993**, *32*, 653.